ACS OMEGA

http://pubs.acs.org/journal/acsodf

Article

Shape-Memory Polymer Nanocomposites of Poly(ε-caprolactone) with the Polystyrene-*block*-polybutadiene-*block*-polystyrene-tri-*block* Copolymer Encapsulated with Metal Oxides

Sithara Gopinath, Nayarassery N. Adarsh, Pankajakshan Radhakrishnan Nair, and Suresh Mathew*

Cite This: *ACS Omega* 2021, 6, 6261−6273

Read Online

ACCESS | Metrics & More | Article Recommendations | Supporting Information

ABSTRACT: Shape-memory polymer composite (SMPC) blends with thermo-responsive shape memorizing capability have received increasing interest and have been a grooming research area due to their various potential applications. In this work, we report three thermo-responsive SMPCs derived from poly(ε-caprolactone) (PCL) and the polystyrene-*block*-polybutadiene-*block*-polystyrene-tri-*block* copolymer (SBS) encapsulated with CuO, Fe_2O_3, and $CuFe_2O_4$, namely, **SMPC−CuO**, **SMPC−Fe_2O_3**, and **SMPC−$CuFe_2O_4$**, respectively. We have also synthesized the neat shape-memory polymer matrix **SMP** in the context of the effect of the metal oxide encapsulates on the shape-memory property. Neat SBS rubber and PCL are used as the polymer-elastomer blend matrix to form **SMP**. The objective of this study is to understand the effect of these three metal oxide nanofillers encapsulated within the **SMP** matrix and their thermal, mechanical, and shape-memory properties. Morphological, thermal, mechanical, and shape-memory properties of the prepared SMPCs are completely characterized. It is revealed that the addition of nano-metallic-oxide fillers into the polymeric matrix significantly improved the overall properties of SMPCs. The tensile test confirmed that **SMPC−$CuFe_2O_4$** possesses a high tensile modulus and is found to be very rigid when compared to other SMPCs. The shape fixing property is found in the increasing order as follows: **SMPC−CuO** > **SMPC−Fe_2O_3** > **SMP** > **SMPC−$CuFe_2O_4$**. The better thermal, mechanical, and shape-memory performances were shown by the **SMPC−Fe_2O_3** composite, and thus, it can be considered as the better shape-memory polymer nanocomposite among all others. An optimum storage modulus was attained by **SMPC−Fe_2O_3** among the SMPCs. More interestingly, we have developed a microvalve actuator system using **SMPC−Fe_2O_3**, which could be useful for promising microsystem applications.

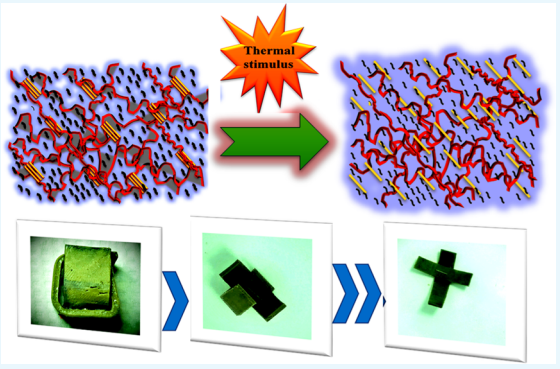

INTRODUCTION

Shape-memory polymers (SMPs)[1−6] are smart stimuli-responsive polymeric materials, which can be programmed to a specific temporary shape and recover their memorized permanent shape upon the application of external stimuli such as temperature,[7−9] light irradiation,[10−12] solvents,[13,14] electrical current,[15,16] magnetic field,[17] and electromagnetic field.[18] SMPs are formed by the cross-linking of polymeric networks, which control the network chain mobility to fix and release the strain. Such cross-linking assists the polymer to make the network structure intact during deformation and allows it to return to the original shape, stimulated by various external responses. The shape-memory effect of any SMP is determined by various factors such as its chemical content and structure, the extent of cross-linking of the polymeric networks, the molecular weight of the monomer unit, and the percentage of the crystalline or amorphous material present in the polymer. Thermo-responsive one-way SMPs,[19] which can switch their shape or elastic network with the interaction of temperature above their melting temperature (T_m) or glass-transition temperature (T_g), attracted many material chemists due to their various potential applications in actuators,[20] self-healing materials,[21] biomedicine,[22,23] and aerospace engineering.[24] Moreover, thermo-responsive SMPs can also be stimulated by indirect heating methods such as electricity, magnetism, light, and radiation (radio or microwave).[25−27] Although SMPs are well accepted as smart polymeric materials due to their intriguing characteristics such as large deformation, a low density, various stimulation methods, and good biocompatibility, they have many limitations when exposed to many applications, mostly in engineering.[28] To overcome these disadvantages, shape-memory polymer nanocomposites (SMPNCs) have been developed.[29−32] The significance of

Received: December 1, 2020
Accepted: February 11, 2021
Published: February 22, 2021

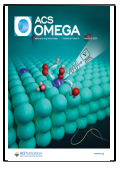

SMPNCs is evaluated in terms of three aspects: reinforcement capability-modified driving methods, creation of specific deformations, and multifunctional materials. Recently, SMPNCs found many applications in the fields of aerospace, biomedical equipment, textiles, actuators, and flexible electronics.[33−36] The major advantages of SMPNCs include establishing their ability to undergo active driving and deformation, adaptiveness, ease of transport, and their rapid production capacity. These validate the unique advantages of SMPNCs in solving problems in many potential applications.[37,38]

SMPNCs are nanocomposites synthesized by the encapsulation of one or more nanofillers within the polymeric host matrix.[39] Recently, many research groups have devoted their efforts to synthesize SMPNCs encapsulated with nanofillers by using the reported SMPs to improve the mechanical, functional, and shape-memory properties. Interestingly, such SMPNCs showed greater stiffness and tensile strength than pure SMPs, which help to overcome the problems associated with such shape-memory materials.[40,41] Important examples of nanofillers used for the construction of SMPNCs are carbon nanotubes,[42] carbon nanofibers,[43] metal oxides,[44] noble-metal-based nanostructures,[45] and cellulose nanocrystals.[46] Studies on iron oxide,[47] neodymium magnet (NdFeB) particles, nickel powder (ZnNi), or ferromagnetic particles have also been reported.[39,48,49]

Among various polymers, poly(ε-caprolactone) (PCL) has attracted much attention during the past decades because of their excellent mechanical, thermal, and viscoelastic properties and biodegradability. PCL can be easily blended with other polymers, and the resultant polymer blends show an intriguing synergistic effect and are explored in many shape-memory applications.[50−52] In the present work, we report the design, synthesis, and characterization of neat polystyrene-*block*-polybutadiene-*block*-polystyrene-tri-*block* copolymer (SBS)−PCL polymer blend nanocomposites, which are shape-memory polymer composites (SMPCs), namely, **SMP**, and their nanofiller-occluded composites with copper oxide, iron oxide, and copper−iron oxide, namely, **SMPC−CuO**, **SMPC−Fe_2O_3**, **SMPC−$CuFe_2O_4$**, respectively. We have investigated the shape-memory property of all these four nanocomposites in which SBS and PCL act as an elastomer and switch polymer, respectively.[53] Further, we study the effect of the metal oxide nanofillers on the shape-memory property of these polymer nanocomposites. We have used metal oxides to fill the voids of the polymeric matrix and have adopted a new synthetic approach in which the fillers were directly blended within the polymeric matrix of PCL and SBS. We deliberately selected PCL[54] as the switch polymer due to its low melting point (which enables them to show the thermo-responsive shape memory effect), biodegradability, low glass-transition temperature, non-toxicity, and relatively higher thermal degradation temperature.[55,56]

RESULTS AND DISCUSSION

We have taken an equal ratio of SBS and PCL along with 1/5th of nano-metal-oxide fillers such as Fe_2O_3, CuO, and $CuFe_2O_4$, as shown in Table 1. Thus, **SMP**, **SMPC−CuO**, **SMPC−Fe_2O_3**, and **SMPC−$CuFe_2O_4$** were synthesized with this composition separately by blending in a Hakke mixer at 180 °C and 60 min^{-1} (60 rpm) for 7 min. After blending, these samples were collected from the mixer and compressed in mold plates by a hot press method at a temperature of 180 °C

Table 1. Component Ratios of Various Composites

	SMP	SMPC−CuO	SMPC−Fe_2O_3	SMPC−$CuFe_2O_4$
SBS	1	1	1	1
PCL	1	1	1	1
Filler	0	0.2	0.2	0.2

and a pressure of 5 kg N/m^2. The prepared sample films have a thickness of 2.5 mm. The addition of the nano-metal-oxide fillers with the blend resulted in a dark texture to the polymer nanocomposite sheet. Scheme 1 shows the schematic diagram

Scheme 1. Schematic View of the Synthesis of SMPNCs Built from SBS, PCL, and Nano-Metal Oxides

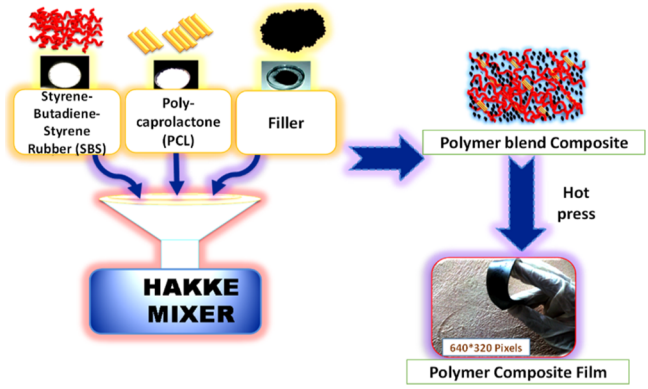

of the synthesis of SMPNCs. The film obtained is characterized by Fourier transform infrared (FT-IR) spectroscopy, UV−visible (UV−vis) spectroscopy, X-ray diffraction (XRD), TGA, DSC, etc.

FT-IR has been widely used to study the mechanism of polymer degradation because it analyzes the intensities of various functional groups as a function of temperature and time. Figure 1 shows the FT-IR spectrum of various shape-

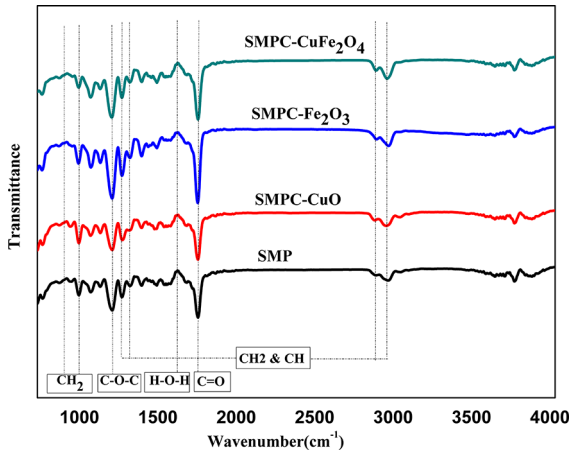

Figure 1. FT-IR spectrum of various SMPNCs.

memory polymer blends such as **SMP**, **SMPC−CuO**, **SMPC−Fe_2O_3**, and **SMPC−$CuFe_2O_4$**. The spectrum was recorded in the wavenumber range of 400−4000 cm^{-1}. All spectra appeared to be almost identical, with only a slight difference in intensity of the transmittance peak. The stretching vibrations of polystyrene (PS) units were present at 540−570, 1028, 1070, 1154, 1238, and 1266 cm^{-1}. The FT-IR

https://dx.doi.org/10.1021/acsomega.0c05839
ACS Omega 2021, 6, 6261−6273

frequencies due to bending and stretching vibrations of polybutadiene (PB) units were also visible at 727, 966, 1238, 1403, 1639 (C═C), 1650, and 2910 cm^{-1}. The vibration bands within the ranges of 2941−2916, 1243−1277 cm^{-1} (CH_2 and CH stretching vibrations), and 946−818 cm^{-1} (due to CH_2 chain vibrations) were attributed to PCL. Similarly, the FT-IR band at 1170 cm^{-1} belongs to the symmetric C−O−C stretching vibration. A weak band centered at 1612 cm^{-1} is due to H−O−H bending vibrations in the composites, and the broad band at 667 cm^{-1} is assigned to C═O vibrational stretching. Carbonyl stretching (C═O), which represents the characteristic absorption peaks of PCL, was observed at 1726 cm^{-1}.[71]

UV−vis spectroscopy is considered to be one of the important characterization techniques to study and analyze the optical properties of polymer nanocomposites. Spectrophotometric data were recorded at room temperature in the 200−800 nm range. Using this, we can easily understand the interaction between the matrix and the nanofillers and thereby study the role of nanofillers in enhancing their property in the form of nanocomposites. Compared with other characterization techniques, UV−vis spectroscopy is one of the valuable tools to evaluate the optical properties of various nanofillers in a polymer matrix. Figure 2 shows the UV spectrum of blend

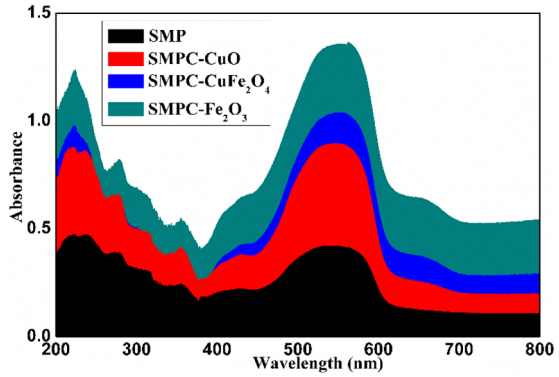

Figure 2. UV spectrum of various SMPNCs.

nanocomposites. The spectrum shows a high absorption peak in the wavelength range of 240−550 nm. The polymer PCL shows a broad absorbance band at 200−250 nm due to n−p* transition.[54] During UV illumination on the sample surface from the instrument source, the absorbance peak at λ_{max} = 410 nm is assigned to the p−p* transition of the polymer−elastomer, whereas the absorbance peak approximately at λ_{max} = 550 nm corresponds to the n−p* transition of the polymer nano-metal-oxide composite.[56]

XRD is an excellent technique to investigate the degree of crystallinity of any semi-crystalline, amorphous polymeric, and composite materials. Figure 3 shows the XRD pattern of the neat matrix and also the nano-metal-oxide-reinforced polymer elastomer blend matrix SMPCs.

In the neat SMP matrix, a broad peak was observed at 10.8° 2θ, which represents the amorphous nature of SBS rubber. On the other hand, sharp peaks were also found at 21.43, and 23.55° positions, which could be due to the orthorhombic PCL polymer reflections, which are depicted as (1 1 1) and (2 0 0) crystal planes, respectively.[71] Metal-oxide-filled **SMPNCs** show small vibrations near 37°, which is common in oxide composites. The crystalline peak of PCL was found to be

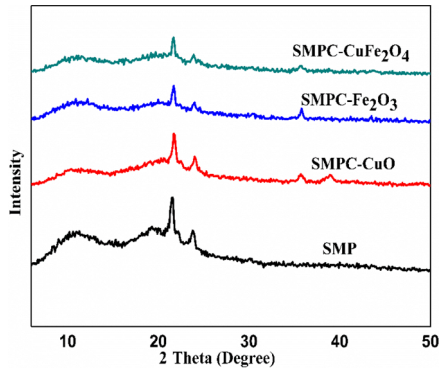

Figure 3. XRD spectrum of various SMPCs.

diminished when the **SMPNCs** were reinforced with the fillers. This is because the crystalline nature of the materials decreases with the occlusion of metal oxides within the polymeric matrix.

Thermogravimetry with coupled gas chromatography−mass spectrometry (TG−GC−MS) is an ideal tool to detect the evolved volatile gases from pyrolyzed samples under specific conditions.[60−63] During TG−GC−MS studies, TG is used to analyze the mass change and GC−MS is used to separate and identify the components of the evolved volatiles. Kinetic models are usually used to analyze the complex pyrolysis kinetics. The pyrolysis kinetics and behavior of various samples are analyzed using TGA and derivative thermogravimetry (DTG) analysis. The TGA and DTG curves of SMPCs are shown in Figure 4a,b. Figure 5a−d shows the corresponding MS plots of **SMP**, **SMPC−CuO**, **SMPC−Fe_2O_3**, and **SMPC−$CuFe_2O_4$**, respectively.

The phenomenological details regarding the temperature of inception (T_i), the temperature of completion (T_f), and the temperature of summit (T_s) for the thermal degradation of

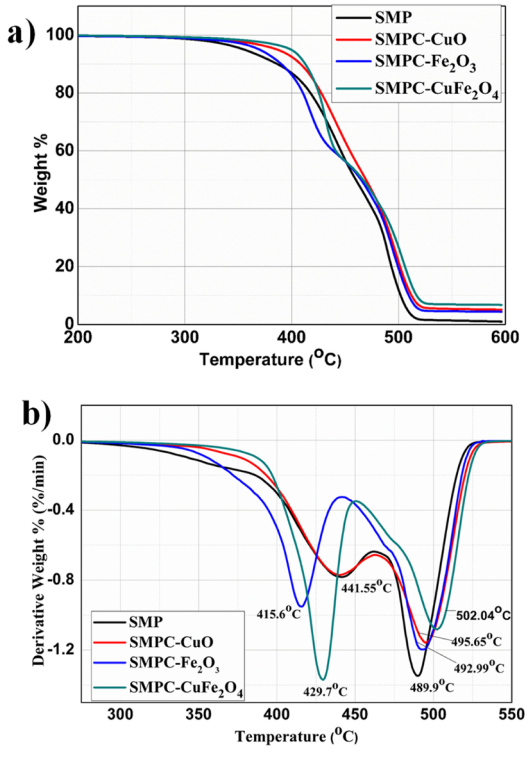

Figure 4. (a) TGA and (b) DTG curves of different samples.

https://dx.doi.org/10.1021/acsomega.0c05839
ACS Omega 2021, 6, 6261−6273

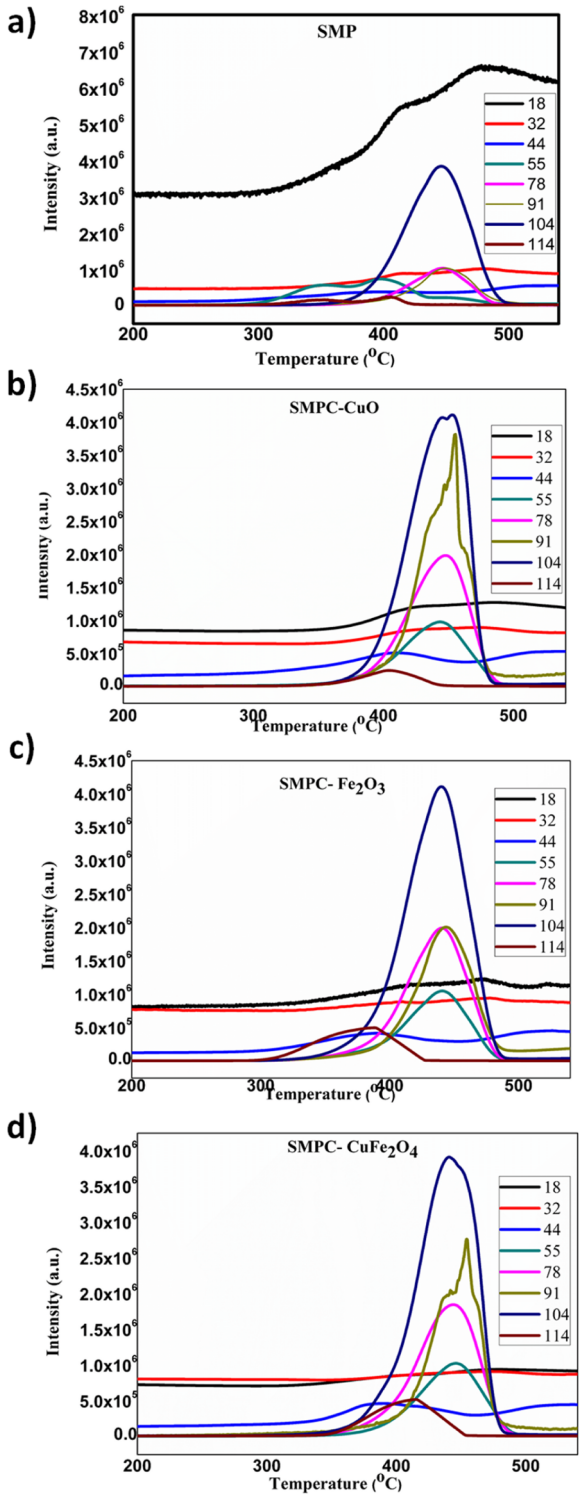

Figure 5. MS plots of different samples: (a) **SMP**, (b) **SMPC−CuO**, (c) **SMPC−Fe_2O_3**, and (d) **SMPC−$CuFe_2O_4$**.

differently prepared samples at 5 °C/min are shown in Table 2. The results show that polymeric SMPCs have undergone thermal degradation in two different stages.[64]

Pyrolysis of different SMPCs can be divided into two stages. The first stage (I) represents the weight loss due to water content, carbon dioxide, and carboxylic acids. The second stage (II) refers to the rapid thermal decomposition between

Table 2. Phenomenological Data for Thermal Decomposition of Various Samples

		decomposition behaviour			
samples	stage	T_i (°C)	T_s (°C)	T_f (°C)	% weight loss observed
SMP	**I**	**300**	**441.5**	**462**	**42.43**
	II	**462**	**489.9**	**600**	**55.36**
SMPC-CuO	**I**	**300**	**441.5**	**462**	**35.17**
	II	**462**	**495.6**	**600**	**58.44**
SMPC-Fe_2O_3	**I**	**300**	**415.6**	**441**	**42.43**
	II	**441**	**492.9**	**600**	**52.21**
SMPC-$CuFe_2O_4$	**I**	**300**	**429.7**	**450**	**42.44**
	II	**450**	**502.0**	**600**	**50.14**

400 and 600 °C and corresponds to pyrolysis of the caprolactone monomer, benzene, toluene, etc.

The Coats−Redfern equation is often used to study the kinetic parameters of the pyrolysis process, and this method is one of the most reliable methods for the calculation of the kinetic parameters. The Coats−Redfern equation is given below[65]

$$\ln \frac{g(\alpha)}{T^2} = \ln\left[\frac{AR}{\phi E}\left(1 - \frac{2RT}{E}\right)\right] - \frac{E}{RT}$$

where $g(\alpha) = 1 - (1 - \alpha)^{(1-n)}/1 - n$, n is the order parameter, and α is the extent of decomposition. The linear plots of $\ln[g(\alpha)/T^2]$ against $1/T$ were plotted by taking α and T values from the TG curve. The value of n is taken as 1, which is selected by the best fit having a maximum correlation coefficient. From the obtained linear plots, we can calculate the slope and the intercept, and E and A can be calculated.

The entropy of activation was calculated using the following equation, where K is the Boltzmann constant, h is Planck's constant, and $\langle \Delta S \rangle^{\#}$ is the entropy of activation

$$A = \left(\frac{KTs}{h}\right)\exp\left(\frac{\Delta S^{\#}}{R}\right)$$

Table 3 shows two stages of decomposition and values of r (correlation coefficient), E (activation energy), A (pre-exponential factor), and ΔS (entropy). The effect of heat and mass transfer on the pyrolysis reaction affects the equilibrium of the reaction, and as a result of this, activation energies are found to be higher at the end of the pyrolysis (stage II). Concerning the correlation coefficient (r), the values ranged from 0.90 to 0.99, indicating the reliability of the analysis results of the kinetics.

The gases evolved from the above thermal degradation have been analyzed simultaneously using GC and MS. The extracted m/z values such as 18, 32, 44, 55, 77, 91, 104, and 114 correspond to the evolution of water, oxygen, carbon dioxide, 1,3-butadiene, benzene, toluene, styrene, and ϵ-caprolactone/5-hexenoic acid, respectively (shown in Table 3). The first-stage decomposition of PCL generates water (m/z: 18), carbon dioxide (m/z: 44), and carboxylic acid (5-hexenoic acid, m/z: 114) as evolved products, and decomposition of SBS results in the elimination of moisture and volatiles, as shown in Figure 5. It is observed that there is a significant loss below 200 °C, corresponding to the loss of weakly bonded water (seen in all samples). Water loss is also observed between the temperature of 350 and 550 °C, which is also evident in all prepared samples, due to dehydroxylation in SBS

https://dx.doi.org/10.1021/acsomega.0c05839
ACS Omega 2021, 6, 6261−6273

Table 3. Obtained Values of r and E in Different Stages of Pyrolysis

sample	stage	r (correlation coefficient)	E (activation energy) KJ/mol	$\Delta S^{\#}$ entropy (J/g)	A (S^{-1})
SMP	I	0.90	134.0	−39.25	1.75×10^{9}
	II	0.99	280.6	−36.18	4.54×10^{9}
SMPC-CuO	I	0.98	194.3	−22.87	1.63×10^{11}
	II	0.99	242.9	18.90	1.93×10^{16}
SMPC-Fe_2O_3	I	0.99	166.3	17.26	7.27×10^{11}
	II	0.99	312.5	55.74	5.18×10^{20}
SMPC-$CuFe_2O_4$	I	0.97	236.4	17.00	9.95×10^{15}
	II	0.99	289.8	41.63	1.06×10^{19}

and PCL layers. The water loss is found to be higher in neat SMP and decreases as follows: **SMP** > **SMPC−CuO** > **SMPC−Fe_2O_3** > **SMPC−$CuFe_2O_4$**. Therefore, the water loss due to dehydroxylation is reduced due to the integration of nano-metal-oxide fillers between the layers. The evolution of water is due to the condensation reaction of hydroxyl (OH) and/or carboxylic acid functions *in situ* formed at high temperatures. The thermal degradation of PCL and SBS in an inert atmosphere (helium) occurs due to the rupture of the polyester chain through ester pyrolysis reaction, and it results in the release of CO_2, O_2, and H_2O. All major decompositions and evolutions of gases occurred at a temperature between 350 and 550 °C.

As the pyrolysis continues at higher temperatures, the distinction between ε-caprolactone and 5-hexenoic acid is more difficult as they possess similar molecular fragments: m/z = 114 (molecular ion). ε-caprolactone is a more stable compound compared to 5-hexenoic acid because of the stability imparted due to its ring structure, and also, the boiling point of ε-caprolactone is much higher than that of 5-hexenoic acid. The presence of this monomer unit in the second-stage degradation stage is due to the depolymerization *via* an unzipping mechanism occurring at a temperature above 440 °C.[66] The unzipping depolymerization of PCL chains proceeds by backbiting reaction from the hydroxyl end group onto the ester function of the last monomeric unit.

The possible pyrolysis mechanisms of SBS and PCL are displayed in Scheme 2, and Table 4 shows the evolved products. It can be found that the decomposition of SBS occurs by a free-radical mechanism according to the scission of the polymer.[66,67] Through the chain scission and dehydrogenation reactions, styrene (m/z = 104) and 1,3-butadiene (m/z = 55) are formed, as shown in Figure 5a,b. Benzene derivatives (m/z = 77) and toluene (m/z = 91) are also generated from the styrene ligand.[68] From the graph, it is revealed that the evolution of these gases at major decomposition stage temperatures (350−550 °C) is higher in filler-integrated samples than that of neat ones. The combination of styrene fragments and the butadiene backbone can also lead to the formation of benzene derivatives.[69]

The DSC technique has been widely used to study the phase transitions of polymers and to investigate the response of polymers with temperature, either cooling or heating, which is mainly used to determine the melting temperature (T_m), crystallization temperature (T_c), and glass-transition temperature (T_g) of a crystalline polymer. Figures S1 shows the DSC curves of the samples during heating and cooling modes. T_g and T_c of the polymer elastomer blend and the reinforced nano-oxide film samples were obtained from the DSC curve. The T_g values of the samples of SMPCs were initially from −80 to 135 °C with a heating rate of 10 °C/min. An obvious

Scheme 2. (a) Possible Pyrolysis Mechanism of PCL and (b) SBS

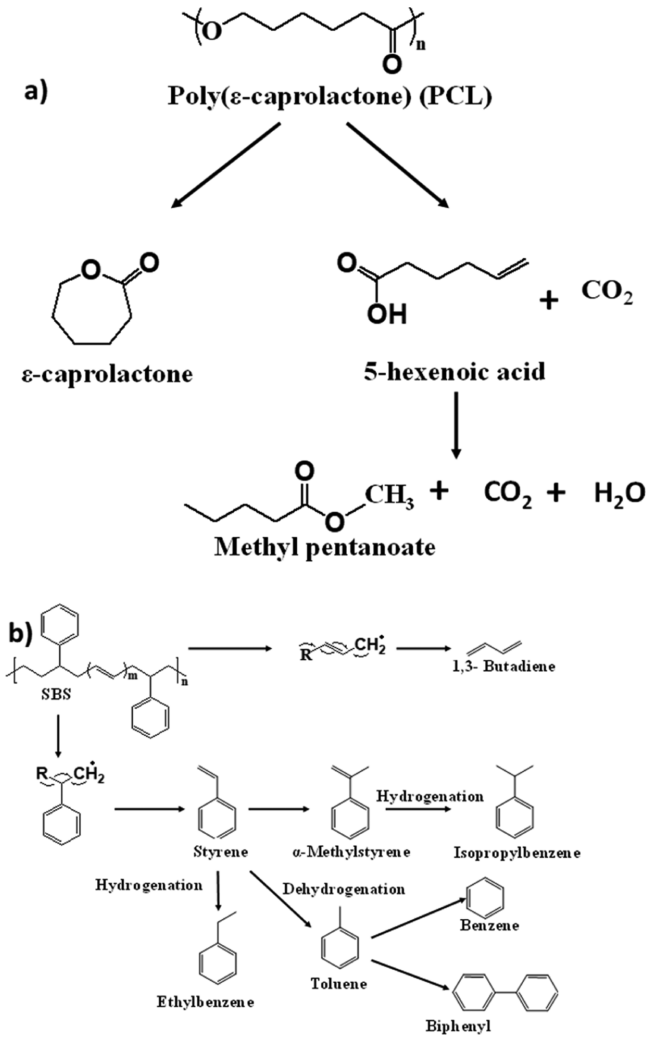

melting temperature, T_m, was observed with the peak temperature at 64 and 63 °C for the metal oxide-occluded SMPCs and neat **SMP**, respectively, in the heating curve. Hence, it is clear that the reinforcement of the nano-oxide fillers into the pure matrix gave a slight positive change in the T_m of the samples. Here, the T_m of PCL is considered as the shape-memory transition temperature (T_{trans}, where the switching between the hard and soft phase occurs) of the pure blend and the nano-oxide-reinforced composite samples. In Figure S2, during cooling, the PCL crystallization occurs and a shoulder peak is found at the range of 40 °C. Since the weight of PCL is taken as the same for all samples, its

https://dx.doi.org/10.1021/acsomega.0c05839
ACS Omega 2021, 6, 6261−6273

Table 4. Details of Evolved Gases During Decomposition

Compound Name	Main m/z	Formula	Structure
Water	18	H_2O	
Oxygen	32	O_2	
Carbon dioxide	44	CO_2	
1,3-Butadiene	55	C_4H_6	
Benzene	77	C_6H_6	
Toluene	91	C_7H_8	
Styrene	104	C_8H_8	
ε-Caprolactone	114	$C_6H_{10}O_2$	
5-Hexenoic acid	114	H_2C=CH(CH2)3COOH	

crystallization occurred at the same temperature, and it is also clear that the fillers did not contribute to any change in this crystallization temperature of the polymer−elastomer blend matrix.

Further, we have characterized the microscopy images of the SMPCs by using polarized optical microscopy (POM), scanning electron microscopy (SEM), and atomic force microscopy (AFM). The surface morphology of prepared SMPCs based on SBS−PCL−metal oxide films is analyzed using the SEM instrument, and Figure 6a−d shows their corresponding SEM images. Figure 6a shows the surface morphology of the neat blend (**SMP**), and the phase difference between SBS and PCL is visible in the image. The physical and chemical properties of SBS and PCL are extremely different. Thus, due to their intrinsic immiscibility, there exist clear and visible phase separations in their phase morphology. Figure 6b shows the SEM image of **SMPC−CuO**. All SMPC films show some macroscopic clusters, and they are in the scattered form throughout the matrix. These clusters could be due to SBS and PCL particles, which remain after melt mixing. Figure 6c shows the SEM images of the **SMPC−Fe_2O_3** polymer nanocomposite film. The particles of SBS and PCL are marked in the SEM images. The uniform-sized nano-iron oxide filler particles are well dispersed in the bulk state. Even though small clusters are visible, the size of clusters is smaller when compared with that of **SMPC−CuO**. Similar clusters are also seen in the SEM images of **SMPC−$CuFe_2O_4$**, as shown in Figure 6d. The figure shows that the fillers are well dispersed in the polymer matrix, indicating strong and better interactions between fillers and the blend matrix. The pure SBS and PCL matrix offered an off-white film due to high-temperature melting and mixing. When the nano-metallic-oxide fillers were added to this pure blend, the color which each filler possesses was transferred to the film. Thus, Fe_2O_3 (which is brown)-blended pure polymer matrix composite films showed a brown texture, CuO blending gave a black texture to the film, and $CuFe_2O_4$ blending offered a dark-brown texture to the films.

POM is the best technique to study the microstructure of solid-state materials. This technique is also used to analyze the crystalline and amorphous nature of the polymer nano-

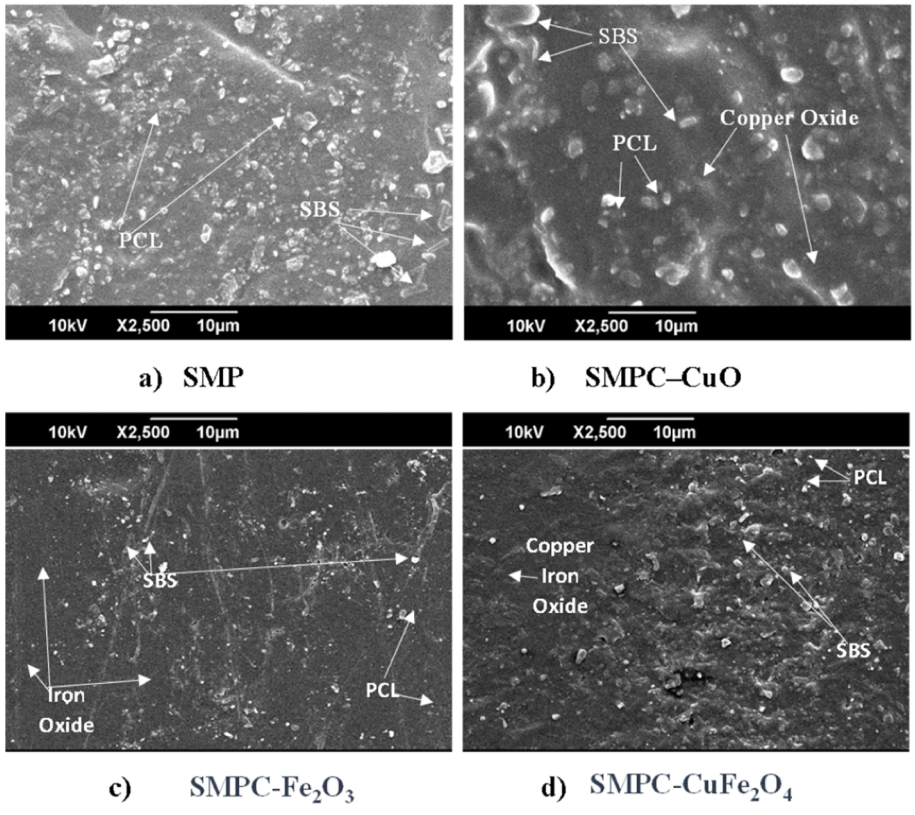

Figure 6. SEM images of various SMPNCs.

https://dx.doi.org/10.1021/acsomega.0c05839
ACS Omega 2021, 6, 6261−6273

composites. POM is considered as a contrast-enhancing technique to evaluate the material compositions using polarized light and the three-dimensional structure of specimens. Figure S2 shows various POM images of polymer nanocomposites, SMPCs, with various metal oxide fillers.

The different SMPNC images are provided with different colors so that their microstructure can be easily visible. POM is a very useful technique to analyze the internal structure of materials when the composite is transparent or the sample is very thin. Since the prepared SMPC film is not much thin to observe through POM, we coated a thin film of each sample on a glass plate's surface using the "Doctor Blade" method. The molten samples were collected immediately after the melt blending in the mixer and then coated on a glass slide and allowed to dry at room temperature. Small dark regions found in Figure S2 were due to the difference in phase morphology of SBS and PCL. Figure S2a−d shows the different POM images of **SMP**, **SMPC−CuO**, **SMPC−Fe_2O_3**, and **SMPC−$CuFe_2O_4$**, respectively. Small agglomerates were seen in the POM images of **SMPC−CuO**, **SMPC−Fe_2O_3**, and **SMPC−$CuFe_2O_4$**. These could be due to the cluster formation of nano-metallic-oxide particles while melt mixing. The hard phase and soft phase in the POM images are obtained as dark and bright regions, respectively. Large clusters could be due to the semi-blended particles of SBS left after mixing, and they are also identified in the images.

Figure 7 shows the AFM topography and phase images with surface roughness profiles. The AFM images clearly show the immiscibility between PCL and SBS (PB and PS segments) in SMPC blends. The immiscibility between the components resulted in the phase separation in blends as a hard phase and soft phase, which are displayed as dark and bright regions in the figure, respectively. From the AFM images, it is difficult to find individual nano-metallic-oxide particles exposed at the surface of the SMPC blends. Phase signals showed fine, phase-separated, and continuous morphologies for all compositions containing PCL and SBS components. Since the amount of PCL and SBS taken here for the preparation of the blend is the same, its bi-continuous morphology will be distributed uniformly through our blend. When analyzing the surface roughness of the samples, we can see significant differences between the pure SBS−PCL samples and other nano-metal-oxide-filled SMPNCs. The surface roughness morphology of nano-metal-oxide-filled SMPCs is more irregular than that of the pure blend, which may be due to the presence of nanofillers in the polymeric network structure.

The mechanical properties of the samples were characterized by using a tensile test. This test is an effective way to study how a composite material reacts with the force applied to it in tension. Figure 8a shows the stress−strain curves of the samples. Tensile modulus is also known as Young's modulus or modulus of elasticity, which can be defined as the ability of the material to withstand in length, when subjected to lengthwise tension or compression. From this figure, it is clear that **SMPC−$CuFe_2O_4$** possesses a high tensile modulus and is found to be very rigid when compared with other SMPCs. The increase in tensile modulus could be due to the rigidity of the nano-$CuFe_2O_4$ filler used. The strong interaction between the polymer and filler is due to the large interfacial area between the particles present in it. The tensile modulus of **SMPC−Fe_2O_3** was found to be higher than that of **SMPC−CuO**. **SMP** was found to be much more elastic when compared with other films and possesses a less tensile modulus

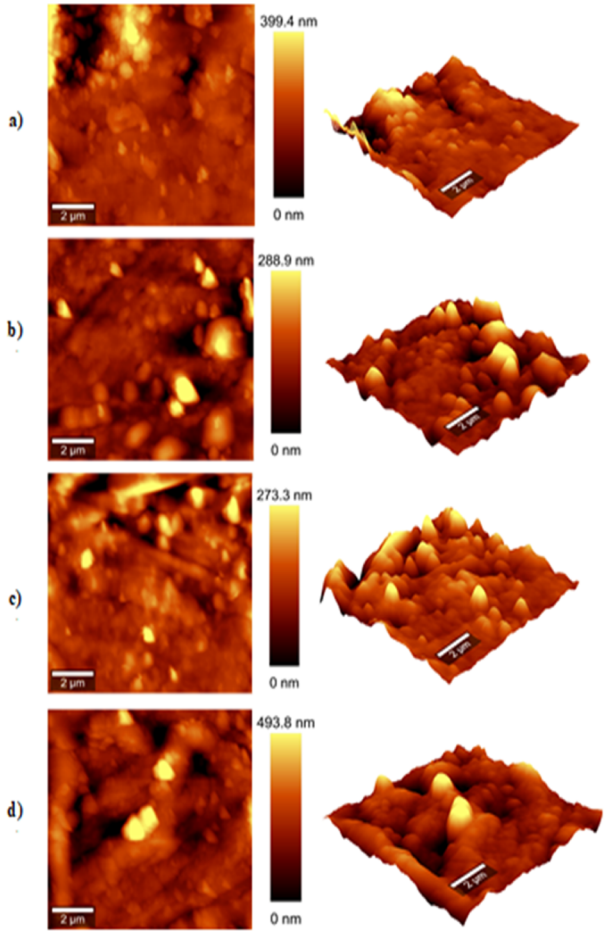

Figure 7. AFM images of (a) **SMP**, (b) **SMPC−CuO**, (c) **SMPC−Fe_2O_3**, and (d) **SMPC−$CuFe_2O_4$**.

value. Young's modulus also measures the resistance to recoverable (elastic) deformation under load. Both of them were considered as mechanical properties of a material. From the tensile study, it is confirmed that **SMPC−$CuFe_2O_4$** possesses high Young's modulus and it changes slightly under elastic loads and resulted in a more brittle nature. On the other hand, the SMP matrix showed low Young's modulus, which implies that it can change its shape considerably like an elastomer. Figure 8b shows the break stress and yield stress of **SMP**, **SMPC−CuO**, **SMPC−Fe_2O_3**, and **SMPC−$CuFe_2O_4$**. Break stress or ultimate tensile stress is defined as the maximum stress experienced on the material before it breaks. From the plot shown in Figure 8b, it is clear that the break stress is prominent in **SMPC−$CuFe_2O_4$**, compared to other SMPCs. Yield stress (σ) or yield strength is defined as the amount of stress required to make a material permanently deformed. Ultimate yield strength or yield point (Y_p), also marked in Figure 8, is defined as the maximum stress that a material can withstand while being stretched or pulled. It was found to be higher for the **SMPC−$CuFe_2O_4$** sample and lower for the neat blend sample, **SMP**.

We have further characterized the shape-memory effect of the SMPCs in response to temperature. Figure 9 shows the shape-memory effect and the process of shape recovery when the samples were placed in hot water of a 90 °C temperature. The box-shaped samples automatically rewind within seconds when placed in hot water, which is due to the shape transition

https://dx.doi.org/10.1021/acsomega.0c05839
ACS Omega 2021, 6, 6261−6273

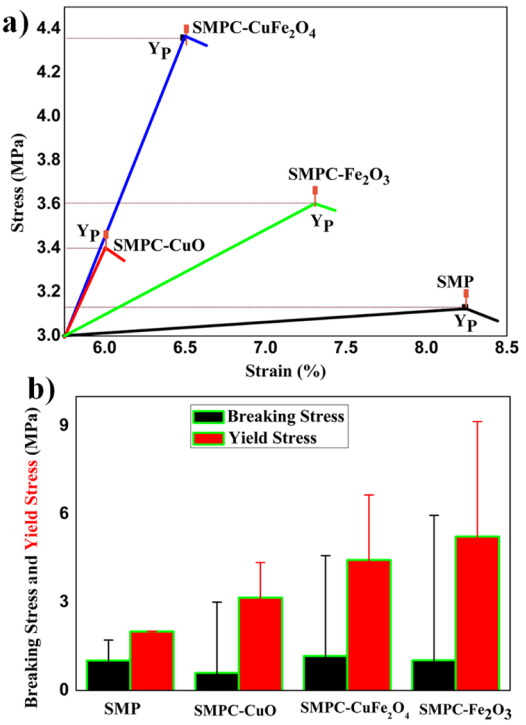

Figure 8. (a) Stress−strain curve; (b) bar diagram for break stress and yield stress of various composite samples. The error bars in the graph represent the standard deviation (n = 5).

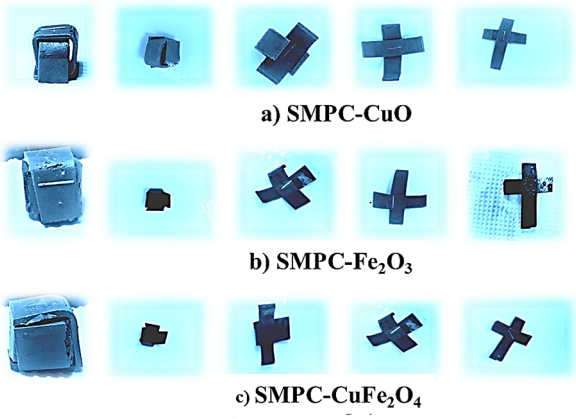

Figure 9. Thermo-responsive shape-memory effect of various samples.

from a temporary shape to a permanent shape. This simple fabrication and the fast recovery process could find many applications in thermo-sensitive sutures, for example, in upcoming research studies. Figure 9a−c shows the shape-memory effect and shape recovery stages of **SMPC−CuO**, **SMPC−Fe_2O_3**, and **SMPC−$CuFe_2O_4$**, respectively. About 95% of shapes have been recovered fast, as shown in the images.

A more detailed analysis of shape-memory properties of the SMPCs is shown in Figure 10a, which displays the shape recovery ratio (R_r) and shape fixing ratio (R_f), concerning the percentage of strain.[41,55,70,71] During the shape recovery of various samples, the values of R_r and R_f were calculated and are illustrated in Figure 10a. The shape recovery ratio (R_r) explains the ability of the sample to memorize its permanent shape. From Figure 10b, it is revealed that the value of R_r is high and equal for **SMPC−Fe_2O_3** and **SMPC−CuO** blend nanocomposite samples with a value of 91.6% and found to be decreasing in the order **SMPC−Fe_2O_3** ≥ **SMPC−CuO** > **SMP** > **SMPC−$CuFe_2O_4$**. The shape fixity ratio (R_f) can be defined as the ability of the switch segments to fix the mechanical deformation. The shape fixing property is found in the increasing order as follows: **SMPC−CuO** > **SMPC−Fe_2O_3** > **SMP** > **SMPC−$CuFe_2O_4$**. Figure 10b shows the recovery time versus the sample plot. From this plot, it is clear that the time taken to recover the original shape by SMP is greater than that taken by **SMPC−Fe_2O_3**, which corroborates well with the shape-memory study, as shown in Figure 10a.

Finally, the shape-memory property of the samples is characterized by using dynamic mechanical analysis (DMA). DMA reveals the effect of temperature on the reinforcing effect in the prepared polymer blend nanocomposites. Dynamic storage moduli (E') of various SMPCs are shown in Figure 11a. Storage modulus represents the mechanical energy stored, stiffness, and shape recovery of the polymer during a loading cycle. For all SMPCs, the nanofiller reinforcement causes a decrease in the dynamic storage moduli over the investigated temperature range, when compared to the neat polymer, **SMP**. G' for the blend composites slightly dropped as the temperature increased from −100 to −80 °C, after which a rapid temperature drop was observed. The rapid decrease is attributed to the glass-transition temperature, T_g (at the range between −65 and −80 °C), of the blend. Generally, the uncompatibilized blend exhibited a higher storage modulus than the compatibilized blend and blend composites.

Compatibilization reduced the storage modulus of the blend due to its rubbery nature. The dynamic storage modulus decreases as follows: **SMPC−$CuFe_2O_4$** > **SMPC−Fe_2O_3** > **SMPC−CuO** > **SMP**. This may be due to the integration of various nano-metallic-oxide fillers into the blend, which obstructs the formation of the cross-links in molecular chain motions. As a result of the postponed chain motions, these polymer chains cannot realign appropriately again, thereby generating further amorphous phases. This implies that more voids are created in the system. Other researchers reported that the polymer chain cross-linking hinders chain packing, consequently leading to an increase in the free volume in the system.[45] The free volumes created as a result of the cross-links are then filled by the oxide fillers incorporated into the system. The optimum storage modulus was attained by **SMPC−Fe_2O_3** among the SMPCs.

The loss modulus analyses revealed the damping behavior of the polymer, which indicates the ability of the prepared polymers to disperse mechanical energy through the internal molecular motions, as shown in Figure 11b.

The DMA loss modulus (E'') is a suitable and beneficial tool to study the shape-memory effect of polymers because it measures the viscous nature of polymeric materials. The peak maximum of E'' relates to the establishment of significant segmental motion of SMPC polymer chains. Loss modulus is a sensitive indicator of molecular differences and has proved very useful in failure investigations. SMP has a high peak of the loss modulus value and can lead to mechanical failure when used in devices (especially for medical applications). All samples possess high loss modulus values at very low temperatures (negative temperature ranges) and possess a broader peak.

Tan δ is a sensitive indicator of the thermal/mechanical conditions that cause significant bond rotation or intermolecular friction and flow. Increasing tan δ generally indicates

https://dx.doi.org/10.1021/acsomega.0c05839
ACS Omega 2021, 6, 6261−6273

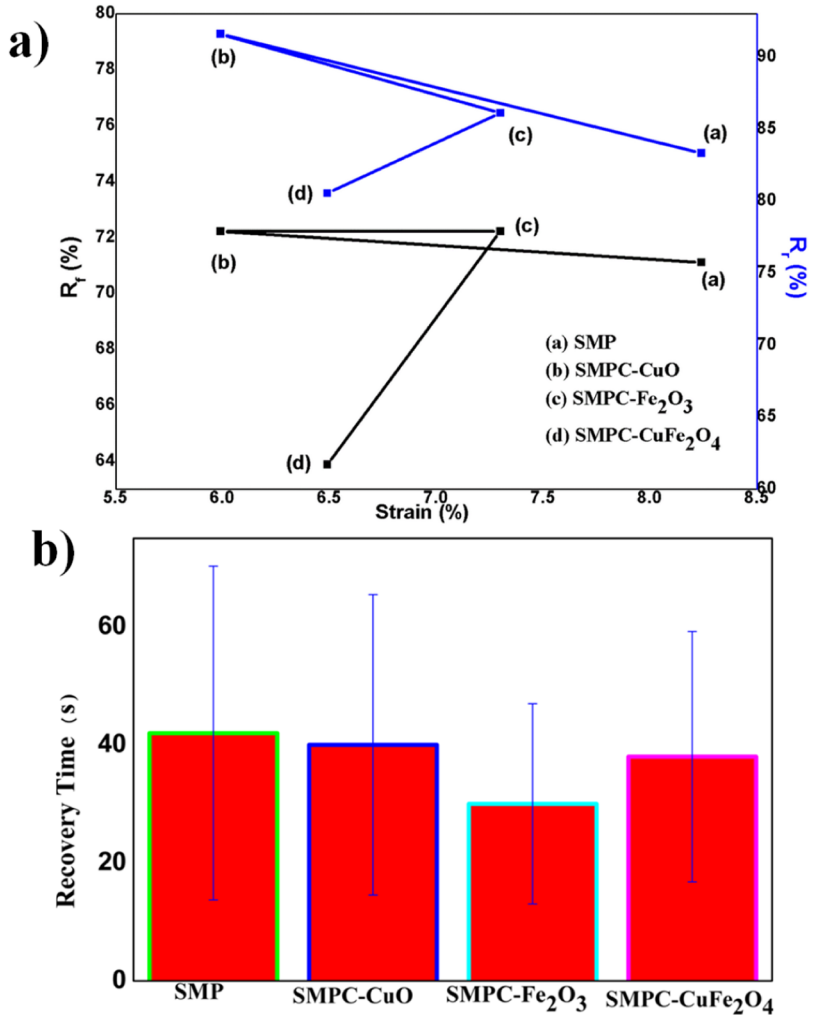

Figure 10. (a) Comparison of thermal shape recovery of various composite samples using thermal shape recovery stages R_r and R_f. (b) Thermal shape-memory analysis using the recovery time of various composite samples. The error bars in the graph represent the standard deviation (n = 5).

that the materials have more energy dissipation potential. Therefore, the greater the tan δ, the more dissipative the material is. On the other hand, decreasing tan δ implies that the material acts more elastic, and by applying a load, it has more potential to store the load rather than dissipating it. Here, in Figure 11c, SMP has the lower value of tan δ and the integration of the nanoparticle content increases the value as nanoparticles impose restrictions against the molecular motion of polymer chains (due to the adsorption of polymer chains on the surface of the particles).

To study the shape-memory application of the samples, we demonstrate an open and close gas microvalve actuator system here, which can regulate the airflow through it (Figure 12). For this, a rectangular-shape **SMPC−Fe_2O_3** film was taken with dimensions of 10 × 2 × 0.3 cm. Figure 12a,c shows the cooled state, and Figure 12b,d shows the heated stage which is the memory stage. SMP is fixed to the setup using silicone springs, which helps the slit to open and close. In the heated stage, the deformed film attains its rectangular permanent shape with the help of elongated springs and thus the slit is in the open form so that air can flow through it. When the springs are heated, it pushes the piston upward due to the shape recovery. When cooled, the silicone spring system reaches the normal form and it presses down the SMPC film before hardening and closes the valve. The balanced action between the two forces of the SMPC and spring system during the heating and cooling processes is responsible for the opening and closing of the valves in the microsystems. We believe that the SMPC actuator system developed by us can assist to engineer new promising microsystems.

CONCLUSIONS

In summary, we have designed and synthesized a series of polymer nanocomposites such as **SMP**, **SMPC−CuO**, **SMPC−Fe_2O_3**, and **SMPC−$CuFe_2O_4$** by using the SBS and PCL polymer blend reinforced with nanofiller metal oxides. From SEM, POM, AFM, and DSC results, the immiscibility between the phase's morphologies of SBS and PCL is revealed. The shape-memory transition temperature or melting temperature is 63 °C for **SMP** and 64 °C for nano-metal-oxide-reinforced SMPCs. The DSC curve showed that the glass-transition temperature is above −70 °C and the crystallization temperature is 40 °C. Mechanical properties of the composites were characterized using tensile test equipment. From the results, it is confirmed that **SMPC−$CuFe_2O_4$** possesses a high tensile modulus and it is found to be very rigid when compared with other SMPCs. The pure matrix possesses a low Young's modulus. Generally, the shape-memory mechanism for this type of polymers blended with nano-metallic-oxide fillers

https://dx.doi.org/10.1021/acsomega.0c05839
ACS Omega 2021, 6, 6261−6273

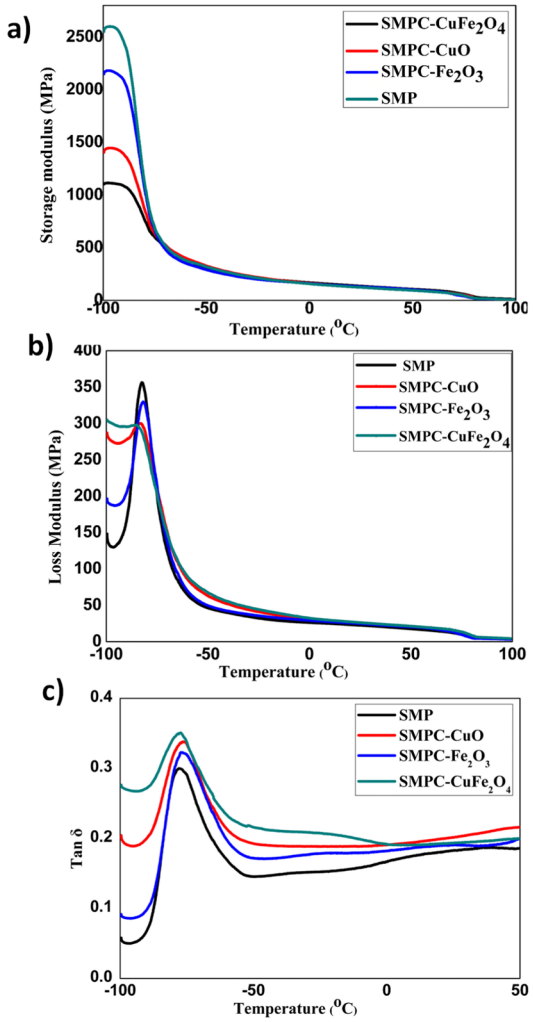

Figure 11. (a) Storage modulus of various composite samples. (b) Loss modulus of various composite samples. (c) Tan δ of various composite samples.

proposed that the two immiscible components of the blend contributed equally to the shape-memory performances. The elastomer SBS provided better stretching, elasticity, and recovery performances, and the PCL switch polymer provided the fixing and unfixing performances. Hence, an optimized design of the phase morphology of the polymer nanocomposite blend is well demonstrated: the major and minor continuous phases are the elastomer and switch polymer, respectively. The values of R_r were high and equal for **SMPC−Fe_2O_3** and **SMPC−CuO** nanocomposite samples with a value of 91.6%. The optimum storage modulus was attained by **SMPC−Fe_2O_3** among the SMPCs. The better thermal, mechanical, and shape-memory performances are shown by the **SMPC−Fe_2O_3** composite, and thus, it can be considered as the better SMPNC among all others.

EXPERIMENTAL SECTION

Materials. Polystyrene-*block*-polybutadiene-*block*-polystyrene (SBS with a trade name MKCF0088, styrene weight 30%) and PCL, with average $M_w \sim 14{,}000$ and $M_n \sim 10{,}000$ by gel permeation chromatography, were purchased from Sigma-Aldrich Chemicals. Nano-metal-oxide fillers such as (i) iron(II, III) oxide nanopowder with a 50−100 nm particle size, (ii) copper iron oxide nanopowder ($CuFe_2O_4$) with a <50 μm particle size, and (iii) copper−iron oxide nanopowder, with a <100 nm particle size (BET) were purchased from Sigma-Aldrich Chemicals and used without any purification or modification.

Characterization. *Scanning Electron Microscopy.* The surface morphologies of oxide fillers and the polymeric phase of the composites were characterized using SEM (JEOL JSM-6390 scanning electron microscope) at 20 kV. A thin layer of gold is coated on the surface of the samples before analysis to get good microscopic images of the composite surface.

Differential Scanning Calorimetry. A differential scanning calorimeter (DSC TA Instruments Q-20 model) was used to investigate the thermal properties of the composite samples. The measurements were done in a nitrogen atmosphere. The 5 mg samples were heated from −100 to 120 °C with a heating rate of 10 °C/min and then isothermally maintained at 120 °C for 5 min; finally, the samples were cooled to 0 °C with a cooling rate of 5 °C/min.

Polarized Optical Microscopy. The phase transition of the composite is also characterized using an optical microscope (Carl Zeiss). Through POM, we can see different brightness regions for regions with different degrees of order of the molecules. Also, the effect of the doping level can be easily analyzed through the 2.5D images.

Atomic Force Microscopy. The surface morphologies of polymeric films were also characterized using an atomic force microscope, WITEC ALPHA, with the 300RA tapping mode and a force constant of 2.8 N/m and resonance with a resonance frequency of 75 kHz.

Fourier Transform Infrared Spectroscopy. FT-IR spectra were recorded on an FT-IR spectrophotometer (IRTracer-100, SHIMADZU). This spectrum helps to analyze chemical functions in materials by detecting chemical bond vibrations and also the interaction between fibers and the matrix in the materials.

X-ray Diffraction. XRD was conducted on a Bench-top X-ray diffractometer (Rigaku miniflex 600) for phase analysis. It helps to identify the crystalline and amorphous regions in the composite.

Thermogravimetry with Coupled Gas Chromatography−Mass Spectrometry. A thermogravimetric analyzer of PerkinElmer, TGA 8000, is used for TG analysis, from 30 to 600 °C in helium (75 mL min^{-1}) at a heating rate of 5 and 1 °C/min. This TGA is connected with a GC−MS system (PerkinElmer Clarus SQ8T) to study the evolved gas during the pyrolysis.

UV−Visible Spectroscopy. UV−vis spectroscopy was carried out on a UV−vis spectrophotometer, UV-2600, at a wavelength of 200−800 nm.

Tensile Tests. Tensile tests were carried out at room temperature using tensile test equipment (TinenSolen, H50KT). The crosshead speed was set at 50 mm/min to make sure that the plots were able to illustrate the toughness or the energy stored in the samples.

Dynamic Mechanical Analysis. The dynamic mechanical properties of prepared samples were determined using a PerkinElmer DMA 8000 in the flexural mode. Samples of rectangular test specimens have the dimensions of 60 mm × 4 mm × 2 mm and were used at a frequency of 1 Hz and a heating rate of 5 °C min in a nitrogen atmosphere. Measurements were performed from −100 to +100 °C. The storage modulus, loss modulus, and tan δ were recorded.

https://dx.doi.org/10.1021/acsomega.0c05839
ACS Omega 2021, 6, 6261−6273

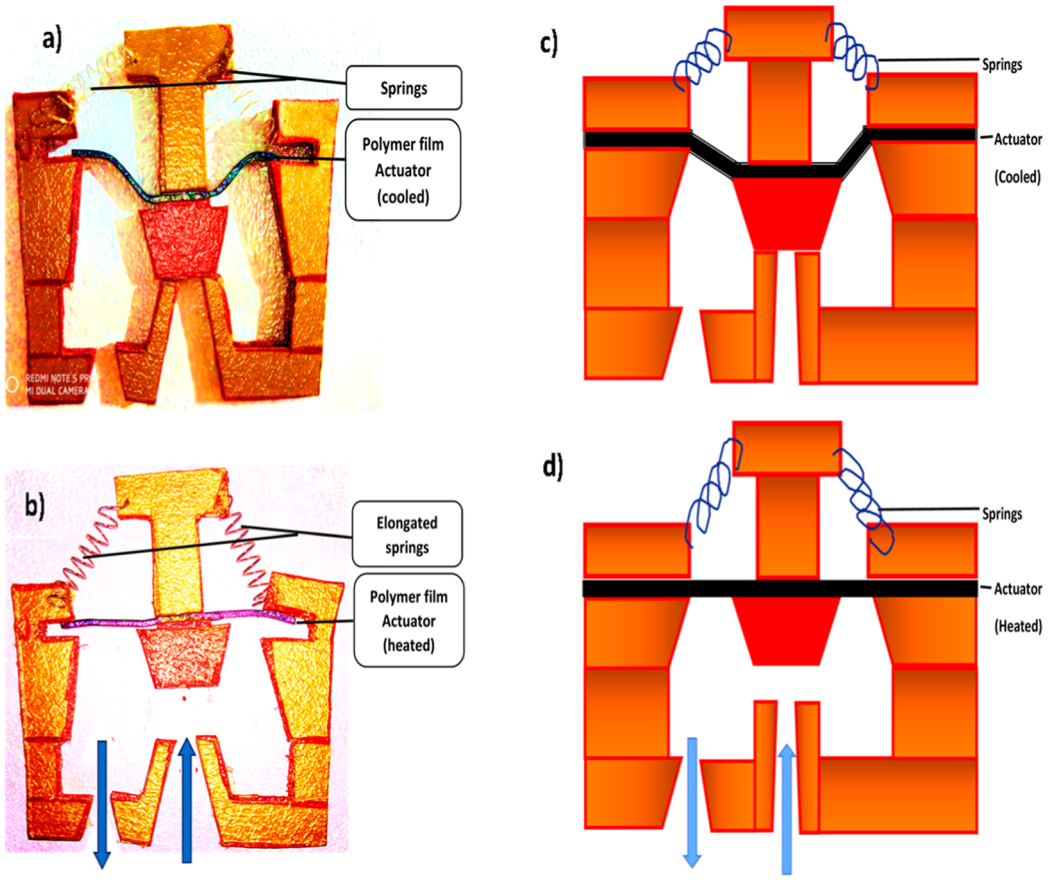

Figure 12. Actuator application of the synthesized SMPC in microsystems: (12a,12c) cooled state and (12b,12d) heated stage.

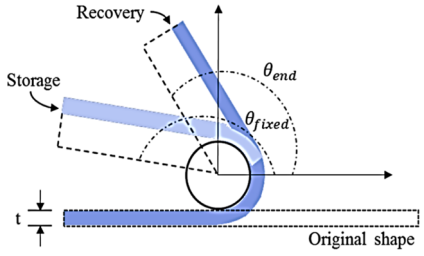

Figure 13. Shape-memory model.

Thermo-Active Shape-Memory Property. The thermo-active shape-memory property was investigated using the "fold-deploy method" on rectangular samples (100 × 10 × 3 mm).[57] The procedure is as follows: (i) the samples were heated to the glass-transition temperature (T_g) in an oven for 5 min. (ii) Then, the samples were taken out and bent into a "U" shape, and a temporary shape is secured. (iii) The "U"-shaped samples were quickly dipped into ice water to maintain the external force generated in it during bending. The deformation angle was recorded as the initial angle (θ_i). (iv) Then, the sample was again placed in a water bath at a temperature higher than T_g, and the shape change was recorded with time (t). Meanwhile, the final angle (θ_f) of the sample was recorded. The temporary shape retention rate (R_f), shape-memory recovery speed (R_s), and shape recovery rate (R_r) were also calculated using the following equations derived from Figure 13.[58,59,72,73]

$$R_f(\%) = \frac{\theta_{\text{fixed}}}{\theta_{\max}}$$

$$R_r(\%) = \frac{\theta_{\max} - \theta_{\text{end}}}{\theta_{\max}}$$

■ ASSOCIATED CONTENT

Supporting Information

The Supporting Information is available free of charge at https://pubs.acs.org/doi/10.1021/acsomega.0c05839.

DSC curves at heating and cooling modes and POM images of SMPCs (PDF)

■ AUTHOR INFORMATION

Corresponding Author

Suresh Mathew − *Advanced Molecular Materials Research Centre (AMMRC), Mahatma Gandhi University, Kottayam, Kerala 686560, India; School of Chemical Sciences, Mahatma Gandhi University, Kottayam, Kerala 686560, India;* orcid.org/0000-0002-7461-3438; Email: sureshmathewmgu@gmail.com

Authors

Sithara Gopinath − *Advanced Molecular Materials Research Centre (AMMRC), Mahatma Gandhi University, Kottayam, Kerala 686560, India*

Nayarassery N. Adarsh − *School of Chemical Sciences, Mahatma Gandhi University, Kottayam, Kerala 686560, India;* orcid.org/0000-0003-2262-8512

https://dx.doi.org/10.1021/acsomega.0c05839
ACS Omega 2021, 6, 6261−6273

Pankajakshan Radhakrishnan Nair − *Advanced Molecular Materials Research Centre (AMMRC), Mahatma Gandhi University, Kottayam, Kerala 686560, India*

Complete contact information is available at: https://pubs.acs.org/10.1021/acsomega.0c05839

Author Contributions

The manuscript was written through the contributions of all authors. All authors have approved the final version of the manuscript.

Notes

The authors declare no competing financial interest.

■ ACKNOWLEDGMENTS

This work was supported by University Junior Research Fellowship from Mahatma Gandhi University. We would like to thank the School of Chemical Sciences (SCS) and the Advanced Molecular Materials Research Centre (AMMRC) for providing us the lab facilities. Also, we sincerely thank our friends, Marilyn Mary Xavior, Soorya Sasi, Gladiya Mani, Sreerenjini.C.R, Olive Abraham, Bhagylekshmi Balan, Sisanth.K.S, and Manukumar.T, for their immense support throughout our work.

■ REFERENCES

(1) Behl, M.; Lendlein, A. Shape-memory polymers. *Mater. Today* **2007**, *10*, 20−28.
(2) Xie, T. Tunable polymer multi-shape memory effect. *Nature* **2010**, *464*, 267−270.
(3) Hager, M. D.; Bode, S.; Weber, C.; Schubert, U. S. Shape memory polymers: Past, present, and future developments. *Prog. Polym. Sci.* **2015**, *49*−*50*, 3−33.
(4) Zheng, N.; Fang, Z.; Zou, W.; Zhao, Q.; Xie, T. Thermoset Shape-Memory Polyurethane with Intrinsic Plasticity Enabled by Trans carbamoylation. *Angew. Chem., Int. Ed.* **2016**, *55*, 11421−11425.
(5) Lendlein, A.; Kelch, S. Shape-Memory Polymers. *Angew. Chem., Int. Ed.* **2002**, *41*, 2034−2057.
(6) Hu, J.; Zhu, Y.; Huang, H.; Lu, J. Recent advances in shape−memory polymers: Structure, mechanism, functionality, modeling, and applications. *Prog. Polym. Sci.* **2012**, *37*, 1720−1763.
(7) Voit, W.; Ware, T.; Dasari, R. R.; Smith, P.; Danz, L.; Simon, D.; Barlow, S.; Marder, S. R.; Gall, K. High-Strain Shape-Memory Polymers. *Adv. Funct. Mater.* **2010**, *20*, 162−171.
(8) Heo, Y.; Sodano, H. A. Self-Healing Polyurethanes with Shape Recovery. *Adv. Funct. Mater.* **2014**, *24*, 5261−5268.
(9) Zhang, G.; Zhao, Q.; Zou, W.; Luo, Y.; Xie, T. Unusual aspects of supramolecular networks: plasticity to elasticity, ultrasoft shape memory, and dynamic mechanical properties. *Adv. Funct. Mater.* **2016**, *26*, 931−937.
(10) Kumpfer, J. R.; Rowan, S. J. Thermo-, Photo-, and Chemo-Responsive Shape-Memory Properties from Photo-Cross-Linked Metallo-Supramolecular Polymers. *J. Am. Chem. Soc.* **2011**, *133*, 12866−12874.
(11) Zhang, H.; Zhao, Y. Polymers with Dual Light-Triggered Functions of Shape Memory and Healing Using Gold Nanoparticles. *ACS Appl. Mater. Interfaces* **2013**, *5*, 13069−13075.
(12) Scott, T. F.; Draughon, R. B.; Bowman, C. N. Actuation in Crosslinked Polymers via Photoinduced Stress Relaxation. *Adv. Mater.* **2006**, *18*, 2128−2132.
(13) Wang, Y.; Heim, L.-O.; Xu, Y.; Buntkowsky, G.; Zhang, K. Transparent, Stimuli-Responsive Films from Cellulose-Based Organogel Nanoparticles. *Adv. Funct. Mater.* **2015**, *25*, 1434−1441.
(14) Liu, Y.; Li, Y.; Yang, G.; Zheng, X.; Zhou, S. Multi-Stimulus-Responsive Shape-Memory Polymer Nanocomposite Network Cross-Linked by Cellulose Nanocrystals. *ACS Appl. Mater. Interfaces* **2015**, *7*, 4118−4126.
(15) Xiao, Y.; Zhou, S.; Wang, L.; Gong, T. Electro-active Shape Memory Properties of Poly(ε-caprolactone)/Functionalized Multi-walled Carbon Nanotube Nanocomposite. *ACS Appl. Mater. Interfaces* **2010**, *2*, 3506−3514.
(16) Khaldi, A.; Elliott, J. A.; Smoukov, S. K. Electro-mechanical actuator with muscle memory. *J. Mater. Chem. C* **2014**, *2*, 8029−8034.
(17) Razzaq, M. Y.; Behl, M.; Kratz, K.; Lendlein, A. Multifunctional Hybrid Nanocomposites with Magnetically Controlled Reversible Shape−Memory Effect. *Adv. Mater.* **2013**, *25*, 5730−5733.
(18) Schmidt, A. M. Electromagnetic Activation of Shape Memory Polymer Networks Containing Magnetic Nanoparticles. *Macromol. Rapid Commun.* **2006**, *27*, 1168−1172.
(19) Kim, Y.-J.; Matsunaga, Y. T. Thermo-responsive polymers and their application as smart biomaterials. *J. Mater. Chem. B* **2017**, *5*, 4307−4321.
(20) Lendlein, A.; Gould, O. E. C. Reprogrammable recovery and actuation behaviour of shape-memory polymers. *Nat. Rev. Mater.* **2019**, *4*, 116−133.
(21) Huang, Y.; Deng, L.; Ju, P.; Huang, L.; Qian, H.; Zhang, D.; Li, X.; Terryn, H. A.; Mol, J. M. C. Triple-Action Self-Healing Protective Coatings Based on Shape Memory Polymers Containing Dual-Function Microspheres. *ACS Appl. Mater. Interfaces* **2018**, *10*, 23369−23379.
(22) Yahia, L. *Shape Memory Polymers for Biomedical Applications*; Woodhead Publishing Series in Biomaterials, 2015.
(23) Serrano, M. C.; Ameer, G. A. Recent insights into the biomedical applications of shape-memory polymers. *Macromol. Biosci.* **2012**, *12*, 1156−1171.
(24) Safranski, D. L., Griffis, J. C. *Shape-Memory Polymer Device Design*; Elsevier and Willam Andrew Applied Science Publishers, 2017.
(25) Mohr, R.; Kratz, K.; Weigel, T.; Lucka-Gabor, M.; Moneke, M.; Lendlein, A. Initiation of shape-memory effect by inductive heating of magnetic nanoparticles in thermoplastic polymers. *Proc. Natl. Acad. Sci. U.S.A.* **2006**, *103*, 3540−3545.
(26) Leng, J.; Lan, X.; Liu, Y.; Du, S. Shape-memory polymers and their composites: Stimulus methods and applications. *Prog. Mater. Sci.* **2011**, *56*, 1077−1135.
(27) Meng, H.; Li, G. A review of stimuli-responsive shape memory polymer composites. *Polymer* **2013**, *54*, 2199−2221.
(28) Rousseau, I. A. Challenges of shape memory polymers: A review of the progress toward overcoming SMP's limitations. *Polym. Eng. Sci.* **2008**, *48*, 2075−2089.
(29) Wu, X.; Han, Y.; Zhou, Z.; Zhang, X.; Lu, C. New Scalable Approach toward Shape Memory Polymer Composites via "Spring-Buckle" Microstructure Design. *ACS Appl. Mater. Interfaces* **2017**, *9*, 13657−13665.
(30) Cai, S.; Sun, Y.-C.; Ren, J.; Naguib, H. E. Toward the low actuation temperature of flexible shape memory polymer composites with room temperature deformability via induced plasticizing effect. *J. Mater. Chem. B* **2017**, *5*, 8845−8853.
(31) Gall, K.; Dunn, M. L.; Liu, Y.; Finch, D.; Lake, M.; Munshi, N. A. Shape memory polymer nanocomposites. *Acta Mater.* **2002**, *50*, 5115−5126.
(32) Li, W.; Liu, Y.; Leng, J. Shape memory polymer nanocomposite with multi-stimuli response and two-way reversible shape memory behaviour. *RSC Adv.* **2014**, *4*, 61847−61854.
(33) Chan, B. Q. Y.; Low, Z. W. K.; Heng, S. J. W.; Chan, S. Y.; Owh, C.; Loh, X. J. Recent Advances in Shape Memory Soft Materials for Biomedical Applications. *ACS Appl. Mater. Interfaces* **2016**, *8*, 10070−10087.
(34) Koerner, H.; Price, G.; Pearce, N. A.; Alexander, M.; Vaia, R. A. Remotely actuated polymer nanocomposites—stress-recovery of carbon-nanotube-filled thermoplastic elastomers. *Nat. Mater.* **2004**, *3*, 115−120.

(35) Deng, J.; Zhang, Y.; Zhao, Y.; Chen, P.; Cheng, X.; Peng, H. A Shape-Memory Supercapacitor Fiber. *Angew. Chem., Int. Ed.* **2015**, *54*, 15419−15423.
(36) Li, X.; Serpe, M. J. Understanding the Shape Memory Behavior of Self-Bending Materials and Their Use as Sensors. *Adv. Funct. Mater.* **2016**, *26*, 3282−3290.
(37) Huang, W. M.; Ding, Z.; Wang, C. C.; Wei, J.; Zhao, Y.; Purnawali, H. Shape memory materials. *Mater. Today* **2010**, *13*, 54−61.
(38) Athimoolam, M.; Moorthy, T. V. Polymer Nanocomposite Materials and Shape Memory Applications-A Review. *Procedia Eng.* **2012**, *38*, 3399−3408.
(39) Lu, H.; Lei, M.; Yao, Y.; Yu, K.; Fu, Y. Q. Shape Memory Polymer Nanocomposites: Nano-Reinforcement and Multifunctionalization. *Nanosci. Nanotechnol. Lett.* **2014**, *6*, 772−786.
(40) He, Z.; Satarkar, N.; Xie, T.; Cheng, Y.-T.; Hilt, J. Z. Remote controlled multishape polymer nanocomposites with selective radiofrequency actuations. *Adv. Mater.* **2011**, *23*, 3192−3196.
(41) Gunes, I. S.; Cao, F.; Jana, S. C. Evaluation of nanoparticulate fillers for development of shape memory polyurethane nanocomposites. *Polymer* **2008**, *49*, 2223−2234.
(42) Liu, Y.; Zhao, J.; Zhao, L.; Li, W.; Zhang, H.; Yu, X.; Zhang, Z. High performance shape memory epoxy/carbon nanotube nanocomposites. *ACS Appl. Mater. Interfaces* **2016**, *8*, 311−320.
(43) Lu, H.; Yin, J.; Xu, B.; Gou, J.; Hui, D.; Fu, Y. Synergistic effects of carboxylic acid-functionalized carbon nanotube and nafion/silica nanofiber on electrical actuation efficiency of shape memory polymer nanocomposite. *Composites, Part B* **2016**, *100*, 146−151.
(44) Huang, J.; Cao, L.; Yuan, D.; Chen, Y. Design of Multi-Stimuli-Responsive Shape Memory Biobased PLA/ENR/Fe_3O_4 TPVs with Balanced Stiffness−Toughness Based on Selective Distribution of Fe_3O_4. *ACS Sustainable Chem. Eng.* **2019**, *7*, 2304−2315.
(45) Mishra, S. R.; Tracy, J. B. Sequential Actuation of Shape-Memory Polymers through Wavelength-Selective Photothermal Heating of Gold Nanospheres and Nanorods. *ACS Appl. Nano Mater.* **2018**, *1*, 3063−3067.
(46) Toncheva, A.; Khelifa, F.; Paint, Y.; Voué, M.; Lambert, P.; Dubois, P.; Raquez, J.-M. Fast IR-Actuated Shape-Memory Polymers Using in Situ Silver Nanoparticle-Grafted Cellulose Nanocrystals. *ACS Appl. Mater. Interfaces* **2018**, *10*, 29933−29942.
(47) Urban, M.; Strankowski, M. Shape Memory Polyurethane Materials Containing Ferromagnetic Iron Oxide and Graphene Nanoplatelets. *Materials* **2017**, *10*, 1083.
(48) Hu, J. *Shape memory polymers: fundamentals, advances, and applications*; Smithers Rapra, 2014.
(49) Buckley, P. R.; McKinley, G. H.; Wilson, T. S.; Small, W.; Benett, W. J.; Bearinger, J. P.; McElfresh, M. W.; Maitland, D. J. Inductively Heated Shape Memory Polymer for the Magnetic Actuation of Medical Devices. *IEEE Trans. Biomed. Eng.* **2006**, *53*, 2075−2083.
(50) Koenig, M. F.; Huang, S. J. Biodegradable blends and composites of polycaprolactone and starch derivatives. *Polymer* **1995**, *36*, 1877−1882.
(51) Matzinos, P.; Tserki, V.; Gianikouris, C.; Pavlidou, E.; Panayiotou, C. Processing and characterization of LDPE/starch/PCL blends. *Eur. Polym. J.* **2002**, *38*, 1713−1720.
(52) Rusa, C. C.; Tonelli, A. E. Polymer/Polymer Inclusion Compounds as a Novel Approach To Obtaining a PLLA/PCL Intimately Compatible Blend. *Macromolecules* **2000**, *33*, 5321−5324.
(53) Zhang, H.; Wang, H.; Zhong, W.; Du, Q. A novel type of shape memory polymer blend and the shape memory mechanism. *Polymer* **2009**, *50*, 1596−1601.
(54) Malikmammadov, E.; Tanir, T. E.; Kiziltay, A.; Hasirci, V.; Hasirci, N. PCL and PCL-based materials in biomedical applications. *J. Biomater. Sci., Polym. Ed.* **2018**, *29*, 863−893.
(55) Gupta, A.; Katiyar, V. Cellulose Functionalized High Molecular Weight Stereocomplex Polylactic Acid Biocomposite Films with Improved Gas Barrier, Thermomechanical Properties. *ACS Sustainable Chem. Eng.* **2017**, *5*, 6835−6844.
(56) Kim, J. K.; Basavaraja, C.; Umashankar, M.; Huh, D. S. Effect of honeycomb-patterned structure on electrical and magnetic behaviors of poly(ε-caprolactone)/capped magnetic nanoparticle composite films. *Polymer* **2016**, *87*, 138−147.
(57) Raghunath, S.; Kumar, S.; Samal, S. K.; Mohanty, S.; Nayak, S. K. PLA/ESO/MWCNT nanocomposite: a study on mechanical, thermal and electroactive shape memory properties. *J. Polym. Res.* **2018**, *25*, 126.
(58) Wang, Y.; Tian, W.; Xie, J.; Liu, Y. Thermoelectric Responsive Shape Memory Graphene/Hydro-Epoxy Composites for Actuators. *Micromachines* **2016**, *7*, 145.
(59) Khonakdar, H. A.; Morshedian, J.; Wagenknecht, U.; Jafari, S. H. An investigation of chemical crosslinking effect on properties of high-density polyethylene. *Polymer* **2003**, *44*, 4301−4309.
(60) Fan, F.; Li, H.; Xu, Y.; Liu, Y.; Zheng, Z.; Kan, H. Thermal behaviour of walnut shells by thermogravimetry with gas chromatography−mass spectrometry analysis. *R. Soc. Open Sci.* **2018**, *5*, 180331.
(61) Fedelich, N. A novel TG−GC/MS system: Quantification of low-content styrene-butadiene rubber in natural rubber. *J. Therm. Anal. Calorim.* **2017**, *127*, 947−954.
(62) Striūgas, N.; Skvorčinskienė, R.; Paulauskas, R.; Zakarauskas, K.; Vorotinskiene, L. Evaluation of straw with absorbed glycerol thermal degradation during pyrolysis and combustion by TG-FTIR and TG-GC/MS. *Fuel* **2017**, *204*, 227−235.
(63) Qin, L.; Han, J.; Zhao, B.; Wang, Y.; Chen, W.; Xing, F. Thermal degradation of medical plastic waste by in-situ FTIR, TG-MS and TG-GC/MS coupled analyses. *J. Anal. Appl. Pyrolysis* **2018**, *136*, 132−145.
(64) Rejitha, K. S.; Mathew, S. Thermoanalytical investigations of tris (ethylenediamine) nickel (II) oxalate and sulphate complexes: TG−MS and TR−XRD studies. *J. Therm. Anal. Calorim.* **2010**, *102*, 931−939.
(65) Coats, A. W.; Redfern, J. P. Kinetic Parameters from Thermogravimetric Data. *Nature* **1964**, *201*, 68−69.
(66) Persenaire, O.; Alexandre, M.; Degée, P.; Dubois, P. Mechanisms and Kinetics of Thermal Degradation of Poly(ε-caprolactone). *Biomacromolecules* **2001**, *2*, 288−294.
(67) Castaldi, M. J.; Kwon, E. An Investigation into the Mechanisms for Styrene-Butadiene Copolymer (SBR) Conversion in Combustion and Gasification Environments. *Int. J. Green Energy* **2007**, *4*, 45−63.
(68) Kwon, E.; Castaldi, M. J. Investigation of Mechanisms of Polycyclic Aromatic Hydrocarbons (PAHs) Initiated from the Thermal Degradation of Styrene Butadiene Rubber (SBR) in N_2 Atmosphere. *Environ. Sci. Technol.* **2008**, *42*, 2175−2180.
(69) Vernáez, O.; Dagreou, S.; Grassl, B.; Müller, A. J. Degradation of styrene butadiene rubber (SBR) in anaerobic conditions. *Polym. Degrad. Stab.* **2015**, *111*, 159−168.
(70) Liu, C.; Qin, H.; Mather, P. T. Review of progress in shape-memory polymers. *J. Mater. Chem.* **2007**, *17*, 1543−1558.
(71) Gopinath, S.; Adarsh, N. N.; Radhakrishnan Nair, P.; Mathew, S. One-way thermo-responsive shape memory polymer nanocomposite derived from polycaprolactone and polystyrene-block-polybutadiene-block-polystyrene packed with carbon nanofiber. *Mater. Today Commun.* **2020**, *22*, 100802.
(72) Al-Humairi, S. N.; Majdi, H. S.; Al-Humairi, A. N.; Al-Maamori, M.. Future Prospects: Shape Memory Features in Shape Memory Polymers and Their Corresponding Composites. *InSmart and Functional Soft Materials*; IntechOpen: 2019 Mar 29, p 23.
(73) Wang, Y.-k.; Tian, W.-c.; Zhu, G.-m.; Xie, J.-q. Thermomechanical and shape memory properties of SCF/SBS/LLDPE composites. *Chin. J. Polym. Sci.* **2016**, *34*, 1354−1362.

https://dx.doi.org/10.1021/acsomega.0c05839
ACS Omega 2021, 6, 6261−6273